

Flexible and Robust 2D Arrays of Silver Nanowires Encapsulated within Freestanding Layer-by-Layer Films**

By Ray Gunawidjaja, Chaoyang Jiang, Sergiy Peleshanko, Maryna Ornatska, Srikanth Singamaneni, and Vladimir V. Tsukruk*

Freestanding layer-by-layer (LbL) films encapsulating controlled volume fractions ($\phi = 2.5\text{--}22.5\%$) of silver nanowires are fabricated. The silver nanowires are sandwiched between poly(allylamine hydrochloride)/poly(styrene sulfonate) (PAH/PSS) films resulting in nanocomposite structures with a general formula of $(\text{PAH/PSS})_{10}\text{PAH Ag}(\text{PAH/PSS})_{10}\text{PAH}$. The Young's modulus, toughness, ultimate stress, and ultimate strain are evaluated for supported and freestanding structures. Since the diameter of the nanowires (73 nm) is larger than the thickness of the LbL films (total of about 50 nm), a peculiar morphology is observed with the silver nanowires protruding from the planar LbL films. Nanowire-containing LbL films possess the ability to sustain significant elastic deformations with the ultimate strain reaching 1.8%. The Young's modulus increases with increasing nanowire content, reaching about 6 GPa for the highest volume fraction, due to the filler reinforcement effect commonly observed in composite materials. The ultimate strengths of these composites range from 60–80 MPa and their toughness reaches 1000 kJ m^{-3} at intermediate nanowire content, which is comparable to LbL films reinforced with carbon nanotubes. These robust freestanding 2D arrays of silver nanowires with peculiar optical, mechanical, and conducting properties combined with excellent micromechanical stability could serve as active elements in microscopic acoustic, pressure, and photothermal sensors.

1. Introduction

Particulate reinforced composites are widely utilized in a number of different applications.^[1] The overall property of composite materials is governed by the nature of the reinforcement (e.g., geometry, distribution, interaction between reinforcing materials) and its volume fraction. In dealing with the demand for more compact devices, a similar approach is applied at a much reduced size scale.^[2] For the preparation of ultrathin films, the layer-by-layer (LbL) assembly technique is regarded to be the most versatile approach,^[3] allowing for nanoscale thicknesses and control over the film thickness, internal organization, and molecular structure.^[4] These films can be made into ultrathin nanocomposites with alternating inorganic nanoparticle and polyelectrolyte layers sequentially deposited

on substrates or fabricated as freestanding nanostructures integrated into microfabricated devices.^[5–11] Fabricating freely suspended metal nanoparticle arrays encapsulated in elastic polymer films and integrating them with microfabricated microelectromechanical system (MEMS) structures is a challenging task, which has been accomplished only in a few instances.^[12] A significant reinforcement of micromechanical properties along with a peculiar optical response has been reported for these films, including a stress-dependent Raman response, formation of tunable Raman gratings, unprecedented stabilities, and a self-recovery ability.^[13] Integration of these freestanding structures into silicon-based arrays of optical cavities has enabled thermal imaging by the direct conversion of IR flux into a visible optical response by a photothermal mechanism.^[14]

Nanoparticulate materials with unique stimuli-responsive properties constitute a key component of these prospective sensing elements. For instance, tunable noble metal nanoparticles are often used in ultrathin nanocomposite films.^[15] Silver nanoparticles, known for their intriguing optical properties and biological activity, have been prepared in various well-defined shapes. The available forms of silver nanoparticles include spheres,^[16] cubes,^[17,18] rods,^[19–32] tubes,^[33] prisms,^[34] dendrites,^[35] plates,^[36,37] cables,^[38] and wires with diameters as low as 0.4 nm.^[39] Among the different synthetic methods,^[40] polyol synthesis, which was first introduced in 1989,^[41–43] has been much exploited.^[21,44,45] By changing the ratio between the poly(vinyl pyrrolidone) (PVP) capping agent and the silver nitrate precursor, silver nanoparticles can be obtained in various shapes. These nanometer-sized silver particles possess geometry- and size-dependent tunable optical properties,^[46–50] and ex-

[*] Prof. V. V. Tsukruk,^[+] R. Gunawidjaja,^[+] Dr. C. Jiang,^[+] S. Peleshanko,^[+] M. Ornatska,^[+] S. Singamaneni^[+]
Department of Materials Science and Engineering
Iowa State University
Gilman Hall, Ames, IA 50011 (USA)
E-mail: tsukruk@gatech.edu

[+] Present address: School of Materials Science and Engineering
Georgia Institute of Technology
Love Building, Atlanta, GA 30332 (USA)

[**] The authors thank M. C. LeMieux, M. E. McConney, and H. Ko for technical assistance and invaluable help. The PDMS substrate was generously provided by A. Nolte, MIT. This work is supported by AFOSR, FA9550-05-1-0209 and NSF-NIRT-0506 832 grants.

hibit surface-enhanced Raman scattering (SERS)^[51] crucial for prospective sensing applications.^[8,52–57]

In this study, we have tested the feasibility of incorporating metal nanowires into freestanding elastic structures by using LbL assembly. We have conducted a detailed micromechanical study of the resulting flexible 2D silver nanowire arrays, including the evaluation of the elastic modulus, ultimate strength, and ultimate fracturing behavior (toughness) for a wide range of silver nanowire contents. We demonstrate that a planar array of randomly oriented, scarcely or densely packed silver nanowires is robust enough to sustain significant deformations. Earlier, we have also demonstrated the significant in-plane conductivity of LbL nanoscale membranes when the silver nanowire content exceeds the 2D percolation limit.^[58]

2. Results and Discussion

2.1. Characterization of Silver Nanowires

The UV-vis spectrum of purified silver nanowires in methanol ($<0.2 \text{ mg mL}^{-1}$) reveals two distinctive surface plasmon resonance (SPR) peaks, which are characteristic of 1D nanoparticles with a pentagonal cross section.^[47] The peak at 350 nm resembles bulk silver, while another peak at 380 nm corresponds to the transversal plasmon mode (Fig. 1). The longitudinal plasmon resonance peak is not observed in this spectrum due to the high aspect ratio.^[22,59,60] After LbL deposition on a poly(allylamine hydrochloride)/poly(styrene sulfonate) (PAH/PSS) film, the UV peaks for the resulting (PAH/PSS)₁₀PAH Ag assembly are slightly red-shifted (354 and 392 nm) and the relative intensities are altered due to the changes in the environment (Fig. 1). When the same silver nanowires are fully encapsulated within the LbL film, (PAH/PSS)₁₀-PAH Ag(PAH/PSS)₁₀PAH, the relative intensity of the transversal peak increases. However, the peak positions remain the same, 356 and 391.5 nm. The red-shifting and broadening of the SPR peaks for adsorbed silver nanowires is caused by the aggregation of the nanowires and the difference in dielectric properties of the surrounding medium, as discussed previously for silver nanoparticles.^[59]

The X-ray diffraction pattern of silver nanowires confirms a crystal lattice comprising penta-twinned single crystals with five {100} planes along the surface (Fig. 2a).^[61] The peaks at 38.15, 44.45, 64.1, 77.65, and 81.55° can be assigned to a face-centered cubic (fcc) unit cell, as previously reported in the literature. The unit cell parameter calculated from the peak positions, $a=0.408 \text{ nm}$, corresponds closely to the value for bulk silver.^[62]

Atomic force microscopy (AFM) analysis of different areas with different degrees of surface coverage shows highly dispersed silver nanowires (Figs. 2 and 3). The silver nanowires are estimated to be $73 \pm 11 \text{ nm}$ in diameter (d) from cross-sectional anal-

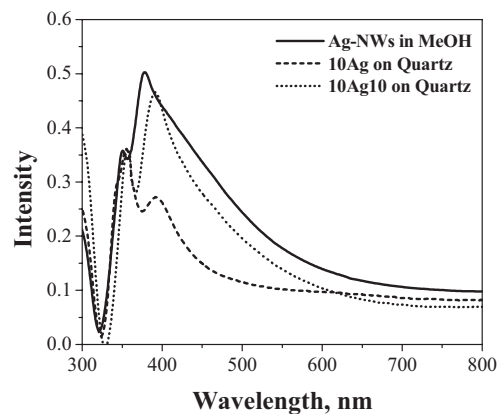


Figure 1. UV-vis spectra for purified silver nanowires in methanol, on a (PAH/PSS)₁₀PAH LbL film, and encapsulated within a (PAH/PSS)₁₀PAH Ag(PAH/PSS)₁₀PAH LbL film (both films are on a quartz substrate).

ysis, with the average length (l) being $6.1 \pm 2 \mu\text{m}$ (Fig. 3). These dimensions give an aspect ratio (l/d) of 84, which is higher than that observed for typical metallic nanorods,^[63] thereby justifying their nanowire nomenclature. Sharply bent and zigzag nanostructures have been occasionally observed in addition to the dominant straight morphology, reminiscent of the structures observed by Chen and Gao in the gold-seeded polyol synthesis of silver nanowires.^[64] High-resolution AFM images re-

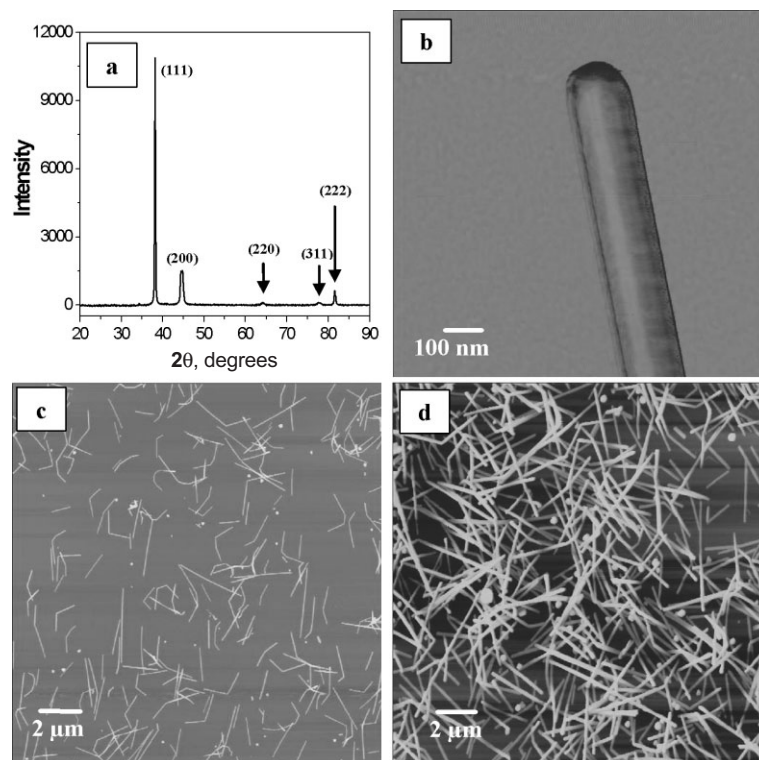


Figure 2. a) A typical X-ray diffraction pattern of films cast from silver nanowire solutions; b–d) AFM images of silver nanowires assembled on ten PAH/PSS bilayers. The Z-scale is 300 nm in (b) and (c), and 800 nm in (d). The volume fraction of silver nanowires (ϕ) is 2.5 % for (c) and 22.5 % for (d).

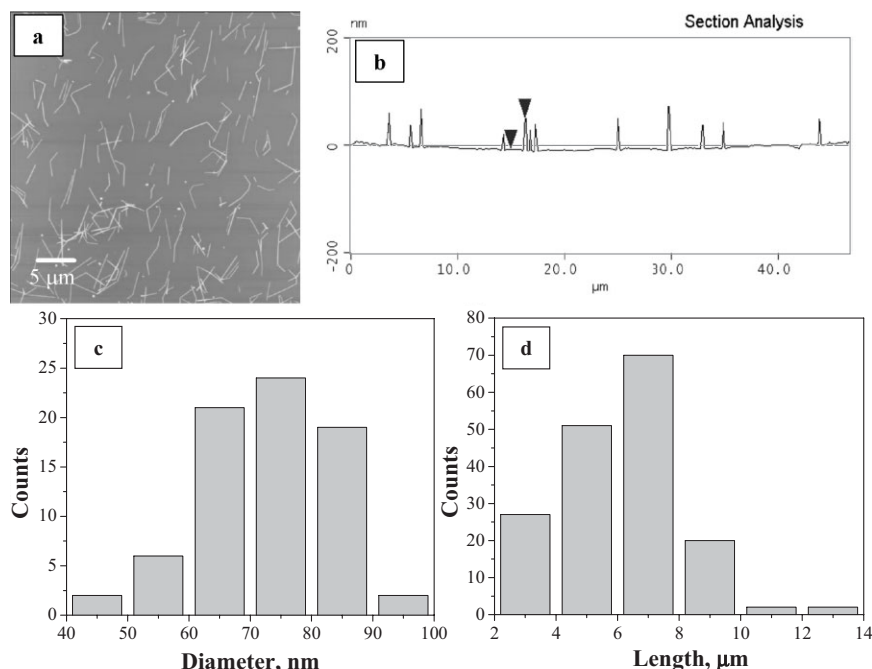


Figure 3. a) AFM topography of silver nanowires deposited on a PAH/PSS/PAH film and b) the corresponding cross-sectional analysis. The Z-scale is 300 nm. c) Diameter and d) length distributions of the silver nanowires.

veal a regular shape with a smooth faceted cross section, as expected for polyol-synthesized silver nanowires (Fig. 2b).^[21,65] The PVP content on the nanowire surfaces is expected to be ca. 3–5 wt % after purification, as reported previously in the literature.^[19] Using a cylindrical core–shell model, we estimate that the thickness of the PVP coating is ca. 4–6 nm, which gives a 61–65 nm diameter for the silver core, which is the value we use to calculate the theoretical composite modulus (see below).

2.2. Controlling the Surface Density of Nanowires

By solution casting different amounts of the nanowire dispersion, silver nanowire arrays with four different surface coverage densities have been prepared on LbL films (Fig. 4, Table 1). The surface coverage is determined by counting the number of nanowires over a $40\ \mu\text{m} \times 40\ \mu\text{m}$ surface area (Fig. 4). The plot of the surface coverage versus number of drops of the nanowire solution used for deposition has been used to determine the surface coverage for the highest density using a linear relationship between the number of drops and the nanowire density. The nanowires predominantly form a random planar array with the vast majority of wires confined to the planar surface and with only modest aggregation even at the highest surface coverage (Fig. 4). The uniform distribution of nanowires without any significant aggregation is preserved after their encapsulation within the LbL films (about 26 nm thick on each side) and upon transfer onto a copper substrate with a microfabricated hole (Fig. 5a). High-resolution optical

imaging shows the random in-plane distribution of silver nanowires, which remain uniform across the edge of the hole (Fig. 5b). AFM images obtained directly for a freely suspended film show a predominantly planar arrangement of silver nanowires coated with the polymer multilayer, along with modest protrusions arising from the larger diameter of the nanowires as compared to the effective thickness of the polymer film (see below) (Fig. 5d). Under certain deposition conditions we have also observed the preferential orientation of silver nanowires in a selected direction, an intriguing phenomenon which is currently under further investigation and will not be discussed further here (Fig. 5c and d).

2.3. Shape of the Freely Suspended Membranes

To elucidate the morphology of freely suspended LbL films with encapsulated silver nanowires, we have directly imaged the top and bottom surface of a region of an LbL film using extremely light tapping mode AFM. The result is the “mirror-like” AFM images displaying identically shaped nanowires shown in Figure 6a and b. Cross-sectional

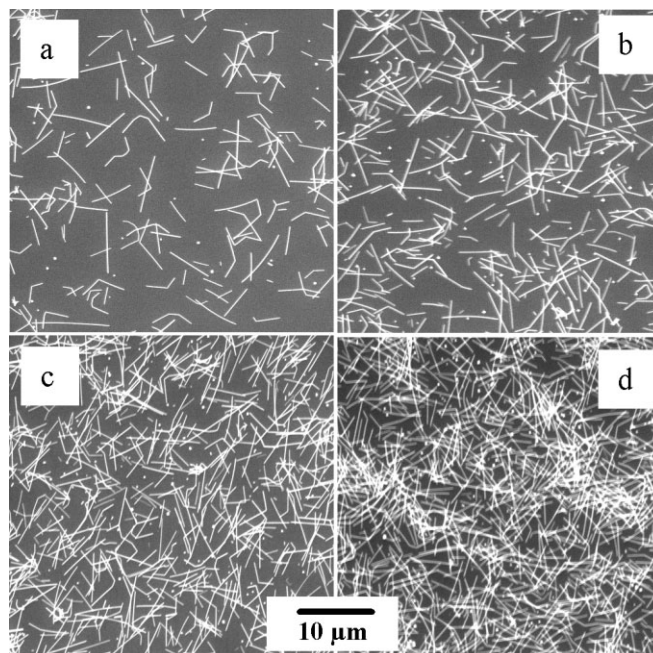


Figure 4. Scanning electron microscopy images of silver nanowires with different surface coverage densities on PAH/PSS/PAH films. The samples have different volume fractions of nanowires, ϕ : a) 2.5, b) 7.5, c) 15, and d) 22.5 %.

Table 1. Effective thickness and Young's moduli of (PAH/PSS)₁₀Ag(PAH/PSS)₁₀ (ϕ) membranes measured from bulging and buckling methods, and calculated from the Halpin–Tsai equation.

Surface area coverage [%]	Volume fraction, ϕ [%]	Effective membrane thickness [nm]	Bulging Young's modulus [GPa]	Buckling Young's modulus [GPa]	Theoretical Young's modulus [GPa]
0.0	0.0	55 ± 2	2.2 ± 0.5	1.7 ± 0.5	2.0
2.1	2.5	46 ± 2	1.6 ± 0.4	2.5 ± 0.5	2.4
6.3	7.5	49 ± 2	2.2 ± 0.5	3.5 ± 0.4	3.2
12.6	15.0	54 ± 2	2.8 ± 0.6	5.0 ± 0.4	4.5
18.9	22.5	60 ± 2	4.6 ± 0.5	5.7 ± 0.5	5.7

protrusion heights on the top and bottom side of the film for the same encapsulated nanowires, as determined by AFM cross-sectional analysis (compare Fig. 6a and b), suggests an asymmetric morphology for the silver nanowires encapsulated within the LbL membrane, as depicted in Figures 6 (top) and 7. A key element of this model is that the silver nanowires are encapsulated within thinner polymer films, where the polymer films conformally cover the nanowires (Fig. 6).

We propose that the asymmetric cross section is caused by the different fabrication conditions for the bottom LbL film assembled on the planar cellulose acetate (CA) substrate and the top LbL film deposited directly onto the silver nanowires.

The protruding portions of the silver nanowires are characterized by different heights **1** and **3** with the film thickness being **2** (Fig. 6). These values have been determined from cross-sectional and bearing analysis of AFM images of both sides of the LbL films, as demonstrated in Figure 8. Surface histograms have also been used to calculate the effective thickness of the LbL film, which is required for the evaluation of the micromechanical properties of the freely suspended films (see below). These dimensions are estimated to be fairly consistent for all LbL films studied here, with values of 45 ± 10 nm for **1**, 44 ± 3 nm for **2**, and 15 ± 2 nm for **3**. These values suggest that the top LbL film conformally covers the nanowires and the nanowires are partially embedded in the bottom supporting LbL film during the assembly process. It is worth noting that the film thickness **2** is only 44 nm, which is less than the thickness of an independently fabricated nanowire-free LbL film (55 nm), indicating that the encapsulation of silver nanowires does indeed affect the overall microstructure in the areas between the particles.

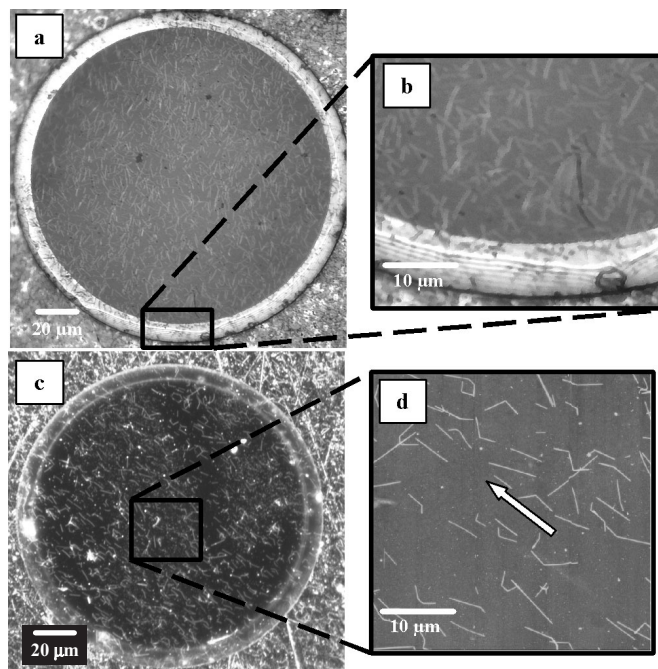


Figure 5. a–d) Representative optical microscopy images of (PAH/PSS)₁₀PAH Ag(PAH/PSS)₁₀PAH films suspended over a 150 μm diameter opening, demonstrating the distribution of nanowires within the LbL films with $\phi = 2.5\%$: a) randomly oriented nanowires with b) a higher magnification image of the film edge; c,d) LbL film with preferentially oriented nanowires; the orientation direction is indicated by an arrow; d) AFM image of the freely suspended membrane shown in (c). The Z-scale is 300 nm. (a) and (b) have been acquired in bright-field mode, while (c) has been acquired in dark-field mode.

analysis of these images reveals that the freely suspended LbL film has a “wavy” contour with elevated features extending beyond the planar nanowire-free surfaces to different extents (see cross sections across identical spots in Fig. 6). High-resolution AFM confirms that the nanowires are completely covered with the PAH/PSS polymer on both sides. The root-mean-square (rms) microroughness of 20 μm × 20 μm surface areas on the top side increases from 15.5 ± 2 nm to 70 ± 6 nm as ϕ increases from 2.5 to 22.5%, while the microroughness of the bottom side increases slightly from 11.9 ± 2 nm to 19.1 ± 2 nm.

This morphology can be understood by considering that the overall diameter of the silver nanowires is 73 nm and the thickness of each (PAH/PSS)₁₀PAH film is only about 26 nm, as determined from independent AFM measurements. The different

2.4. Micromechanical Properties of LbL Films with Encapsulated Silver Nanowires

The bulging test measures the deflection d (in μm) with respect to variable pressure P (Pa) for freely suspended films (Fig. 9). This data has been analyzed using the theoretical model for a circular elastic plate clamped at stiff edges, as previously discussed in detail^[66,67] and defined in Equation 1:

$$P = P_0 + \left[C_0 \frac{E}{1-\nu^2} \frac{h^4}{a^4} + C_1 \frac{\sigma_0 h^2}{a^2} \right] \left(\frac{d}{h} \right) + C_2 \frac{E}{1-\nu} \times \frac{h^4}{a^4} \left(\frac{d}{h} \right)^3 \quad (1)$$

where P_0 is the initial pressure, E is the Young's modulus of the film, ν is its Poisson's ratio, h is film thickness, a is the diameter of the membrane, d is the membrane deflection, and σ_0 is the residual stress. It has been experimentally shown that the

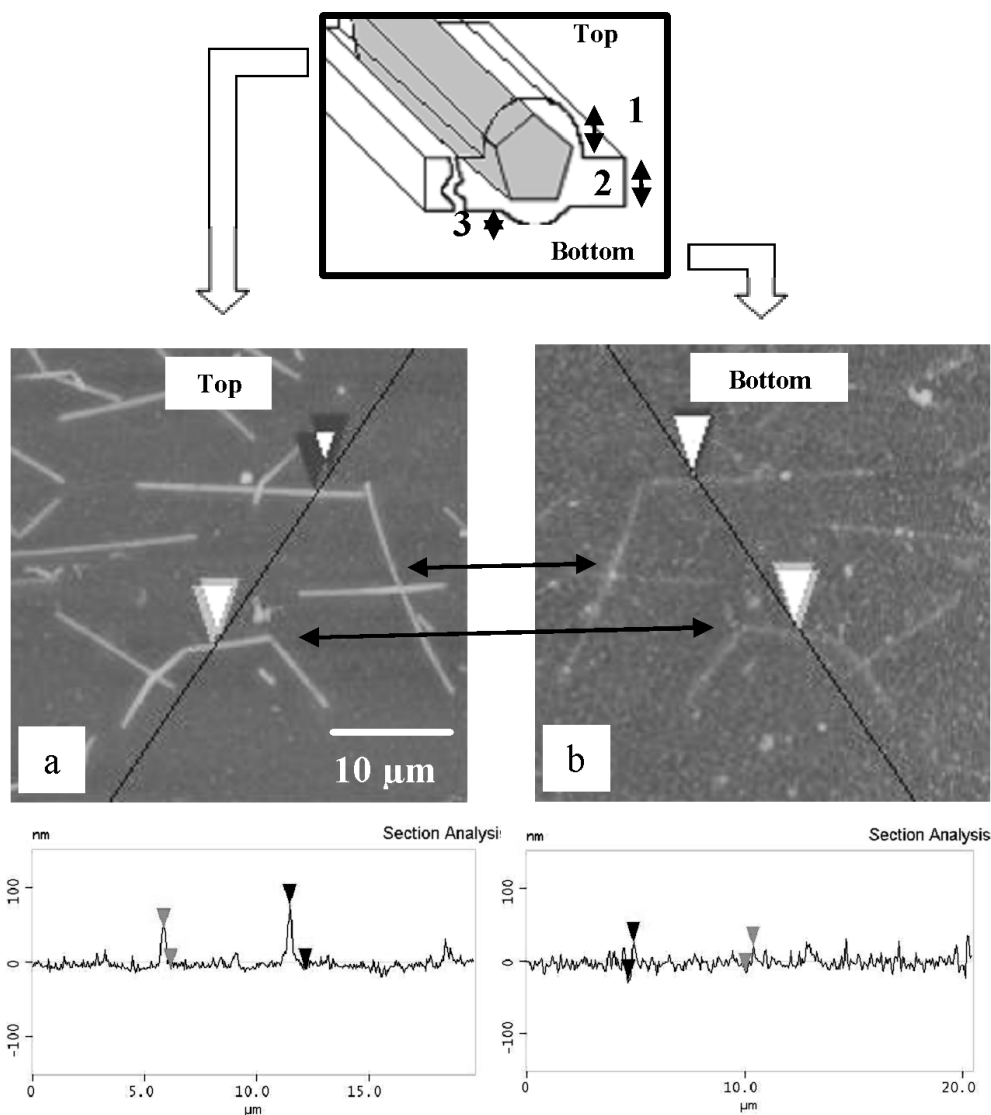


Figure 6. AFM topography image of the a) top and b) bottom surface of a freely suspended (PAH/PSS)₁₀PAH Ag(PAH/PSS)₁₀PAH (2.5 %) membrane, corresponding to the exact same region on both sides along with their corresponding cross sections. Note the mirror symmetry of the images with identical surface features. The top panel is a cartoon representation of an encapsulated nanowire, in which 1 and 3 represent the different protrusion heights of the nanowire and 2 marks the film thickness.

tabulated coefficients C_0 , C_1 , and C_2 are dependent upon the membrane geometry. For a detailed discussion on analyzing this data see Markutsya et al.^[68]

Fitting the experimental data for bulged membranes with different volume contents of silver nanowires allows for the evaluation of their elastic moduli in the tensile regime (Fig. 9). The elastic modulus calculated for the film from Equation 1 increases from 2 to 4.6 GPa with increasing nanowire content (Table 1). The asymmetric microstructure of the nanowire-containing LbL films does not have an influence on the deflection of the film in different directions under positive and negative pressure differentials, as demonstrated in Figure 10, indicating that the major elastic deformation takes place in-between the encapsulated nanowires.

Independent values of the elastic modulus in compression are obtained from the buckling instability test. The overall

buckling pattern is observed to be fairly uniform for different LbL films and the wrinkles are seen to extend over several hundred micrometers (Fig. 11). Smoother surface areas are observed in the vicinity of nanowires, indicating a higher local stiffness; however, this does not affect the overall spacing of the buckling pattern. The Young's modulus of the LbL films, E_{film} , has been calculated from Equation 2, which is valid for uniform polymer films and is used for LbL films as well:

$$\lambda = 2\pi d \left(\frac{E_{\text{film}}(1 - \nu_s^2)}{3E_s(1 - \nu_{\text{film}}^2)} \right)^{\frac{1}{3}} \quad (2)$$

where λ is the spacing of the buckling pattern, d is the film thickness, and E_{film} , ν_{film} , E_s , and ν_s are the Young's moduli and

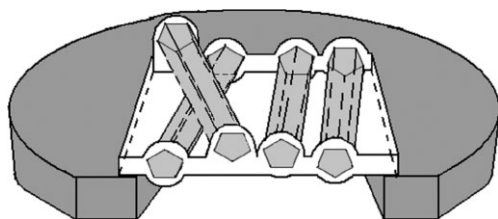


Figure 7. 3D representation of a freely suspended (PAH/PSS)₁₀PAH Ag-(PAH/PSS)₁₀PAH LbL membrane.

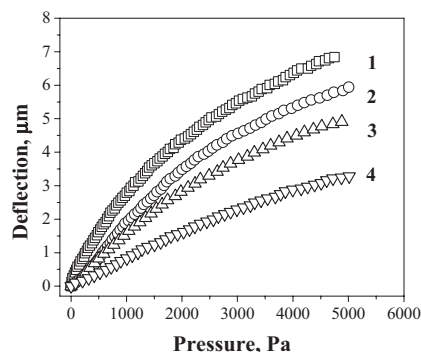


Figure 9. Deflection versus pressure measurements for (PAH/PSS)₁₀-PAH Ag-(PAH/PSS)₁₀PAH membranes as a function of ϕ : 1) 2.5, 2) 7.5, 3) 15.0, and 4) 22.5%.

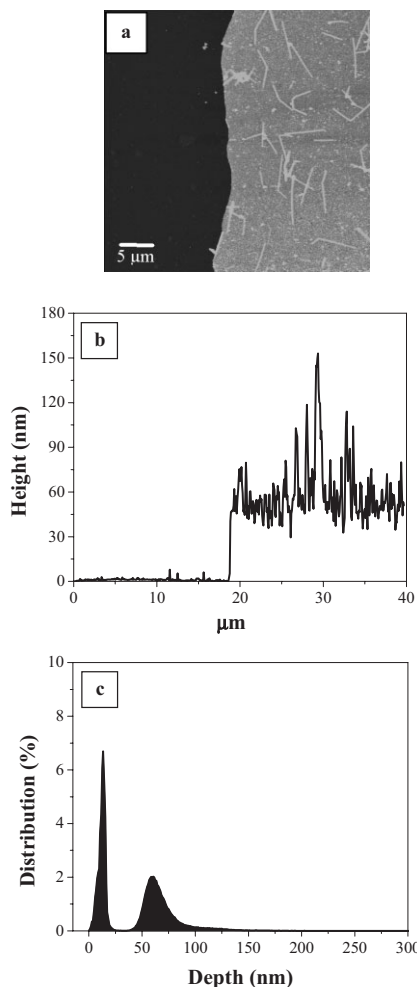


Figure 8. a) AFM image, b) cross section, and c) height histogram of the edge of (PAH/PSS)₁₀PAH Ag-(PAH/PSS)₁₀PAH (2.5%) membrane deposited on a bare silicon wafer. The Z-scale is 500 nm.

Poisson's ratios of the film and substrate, respectively.^[69] The average value of λ , ranging from 2.11 to 3.60 μm for different membranes, has been determined from the 2D Fourier transform of the optical images.^[70] The elastic modulus of the poly(dimethylsiloxane) (PDMS) substrate is 1.8 MPa, as measured by independent tensile stress experiments and confirmed by our AFM force measurements.^[71] The Poisson's ratios for

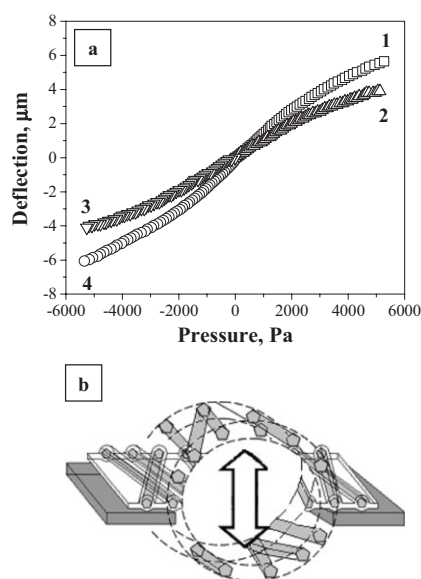


Figure 10. a) Deflection versus pressure plots for (PAH/PSS)₁₀PAH Ag-(PAH/PSS)₁₀PAH (ϕ) membranes: 1,4) $\phi = 2.5\%$, and 2,3) $\phi = 22.5\%$. 1,2) Bulged-up (positive pressure), and 3,4) bulged-down (negative pressure). b) Cartoon representation of the concave and convex shapes of bulging membranes.

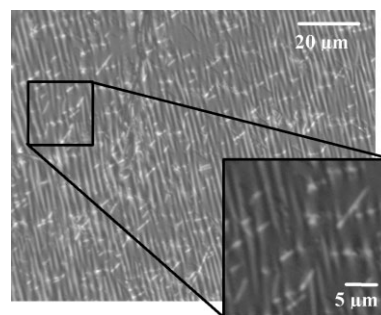


Figure 11. Optical microscopy images of buckling instability for the (PAH/PSS)₁₀PAH Ag-(PAH/PSS)₁₀PAH (2.5%) membrane at different magnifications (differential interference contrast mode).

the LbL membrane and PDMS substrate are assumed to be 0.3 and 0.5, respectively.

The Young's moduli of the LbL films calculated according to Equation 2 increases with increasing silver nanowire content from 1.7 to 5.7 GPa (Table 1). The values obtained for buckled LbL films are fairly close to those for freely suspended LbL films (Fig. 12). All differences observed for LbL films are within or close to the experimental deviation, with the elastic modulus from buckling experiments generally being on the higher

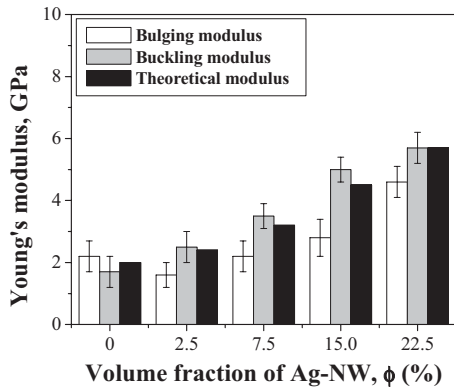


Figure 12. Variation of the Young's modulus as a function of the volume fraction of silver nanowires, ϕ , as evaluated from bulging and buckling experiments, compared to the values estimated for the theoretical composite modulus.

side. The lower elastic modulus for freely suspended LbL films can be attributed to higher residual stresses and a greater role of defects ("weak points") in the tensile deformation of freely suspended films. Therefore, the tensile (bulging experiments) and compressive (buckling) properties of the LbL films are similar, as expected for small elastic deformations of composite materials with randomly oriented 1D fillers.

2.5. Micromechanical Behavior of LbL Membranes with Encapsulated Silver Nanowires

To analyze the micromechanical behavior of nanowire-containing LbL films and the corresponding filler-reinforcement phenomenon, we have employed a Halpin–Tsai model to evaluate the modulus of the composite with randomly oriented fibers, E_{Random} . This model proposes that the composite modulus can be calculated from the Equations 3–7:^[72]

$$E_{\text{Random}} = \frac{3}{8}E_L + \frac{5}{8}E_T \quad (3)$$

$$E_L = \frac{1 + (2l/d)\eta_L V_f}{1 - \eta_L V_f} \times E_m \quad (4)$$

$$E_T = \frac{1 + 2\eta_T V_f}{1 - \eta_T V_f} \times E_m \quad (5)$$

$$\eta_L = \frac{(E_f/E_m) - 1}{(E_f/E_m) + 2(l/d)} \quad (6)$$

$$\eta_T = \frac{(E_f/E_m) - 1}{(E_f/E_m) + 2} \quad (7)$$

where η_L and η_T are the Halpin–Tsai parameters reflecting the ratio of fiber and matrix moduli in longitudinal and transversal directions, respectively, E_T and E_L are the theoretical transversal and longitudinal moduli, which take into account fiber aspect ratio (l/d), fiber volume fraction (V_f), matrix modulus ($E_m = 1.7 \pm 0.5$ GPa for the PAH/PSS film),^[73] and the modulus of silver nanowires ($E_f = 88 \pm 5$ GPa).^[74]

The calculated values of the composite moduli for LbL membranes with different concentrations of nanowires are compared with the experimental values in Table 1 and Figure 12. Note that the volume fraction of silver nanowires used in the theoretical calculation takes into account the core–shell structure discussed above. The Halpin–Tsai calculation shows a systematic increase of the composite modulus with increasing nanowire content, a common feature in filler reinforcement phenomena (Fig. 12). These values are seen to be very close to the experimental ones and virtually coincide with those obtained in the compression mode, indicating that the strengthening of the nanowire-containing LbL films can be explained by the well-known filler-reinforcement phenomenon. The high-aspect-ratio silver nanowires confined within a 2D planar film (Fig. 7) apparently form a dense network even at relatively low nanowire concentrations, significantly enhancing the elastic modulus of the nanocomposite films without considerably affecting their compliance. On the other hand, above a certain critical concentration of nanowires, multilayer networks of nanowires should be predominantly formed, which is indeed observed for the sample with the highest nanowire content tested here. Excessive nanowire junctions and protrusions from the planar film can compromise the integrity of the 2D film and thus the overall micromechanical properties. We suggest that the optimum combination of these two phenomena falls within a narrow window skewed towards lower concentrations of nanowires.

For LbL films that exhibit low ultimate deformation, a full pressure versus deflection curve can be converted into a stress (σ) versus strain (ϵ) curve, which in turn can be used to estimate the film toughness (derived from the area under the stress–strain curve). For a circular geometry, this conversion can be done using relationships^[75,76] $\sigma = Pr^2/4hd$ and $\epsilon = 2d^2/3r^2$, where r is radius of the opening (75 μm), d is the vertical deflection, and h is the film thickness (one example is shown in Fig. 13).^[68] For the most part, the stress–strain curve is linear. Deviation from linear behavior is observed as the deflection of the membrane approaches failure (Fig. 13). This deviation can be attributed to the start of plastic deformation or the yield point of the material. The linear portion of the curve can be expressed as

$$\sigma = \sigma_0 + [E/(1-\nu^2)]\epsilon \quad (8)$$

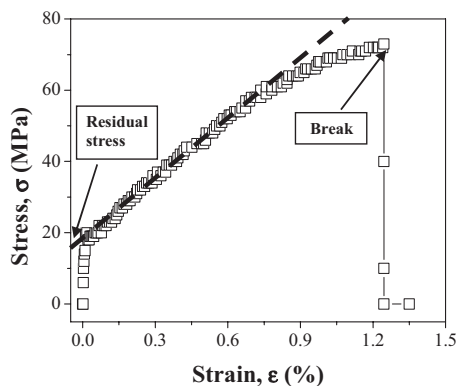


Figure 13. Stress (σ) versus strain (ϵ) plot for the (PAH/PSS)₁₀PAH Ag(PAH/PSS)₁₀PAH (2.5%) membrane. The initial sharp increase results from the residual stress and the final sharp drop is caused by film fracture.

and can be used to calculate the elastic modulus (Fig. 13). The residual stress (σ_0), Young's modulus, ultimate strain (ϵ_{Ult}), ultimate stress (σ_{Ult}), and static fracture toughness (U_t) can all be estimated from the complete stress–strain plots (Table 2). In some cases, the ultimate strain has been obtained without generating the full pressure–deflection curve by extrapolating the partial curve towards the experimentally obtained ultimate pressure at break.

The ultimate strain decreases slightly (from 1.5 to 1.1%) with increasing volume fraction of nanowires, reflecting the higher stiffness due to the presence of the metal filler (Fig. 14). The ultimate stress varies significantly from specimen to specimen but stays within 70 ± 7 MPa for all the compositions studied here. These values are much higher than for purely polymeric LbL films (49 MPa, Fig. 14 and Table 2). On the other hand, these values are comparable to those reported for other reinforced LbL films containing carbon nanotubes and gold nanoparticles.^[7,10,68] Finally, the toughness of the LbL films (total energy required to fracture the film) ranges from 400–1000 kJ m^{-3} with a trend towards lower values for stiffer LbL films and purely polymeric LbL films. The lowest value of 440 kJ m^{-3} for the purely polymeric LbL film is close to that of common glassy polymers,^[77] which is reasonable considering that both the polyelectrolytes in our LbL films are in glassy states at room temperature. The maximum toughness of about 1000 kJ m^{-3} is reached at an intermediate composition (7.5%) due to a combination of higher strength and ultimate strain

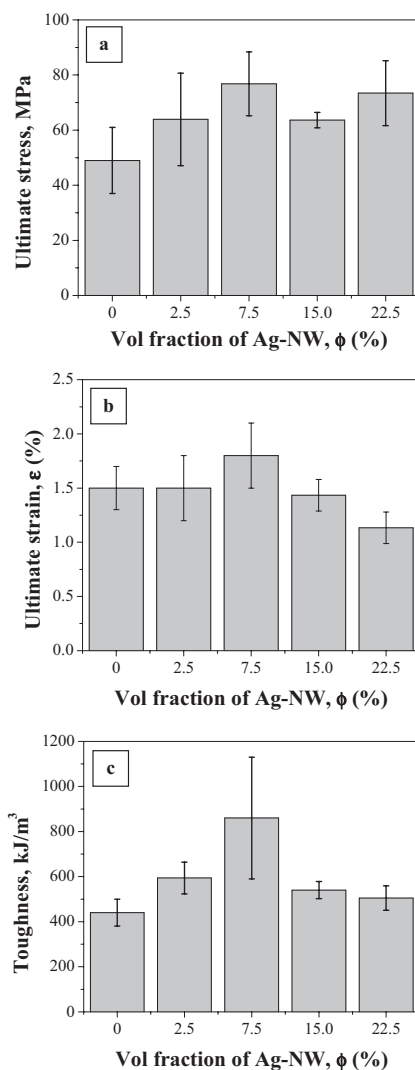


Figure 14. Variation of a) the ultimate stress, b) the ultimate strain, and c) the static fracture toughness as a function of the nanowire volume fraction for (PAH/PSS)₁₀PAH Ag(PAH/PSS)₁₀PAH LbL membranes.

(Fig. 14). This value is on par with tough carbon-nanotube-containing LbL membranes, as estimated from the area under the stress–strain curve.^[8] On the other hand, due to its limited compliance it is still below the record values reachable for partially crystalline tough plastics where high strength is combined with high elasticity and plasticity.^[78]

Table 2. Residual stress (σ_0), ultimate stress (σ_{Ult}), ultimate strain (ϵ_{Ult}), and toughness (U_t) of (PAH/PSS)₁₀Ag(PAH/PSS)₁₀ films.

Nanowire volume fraction, ϕ [%]	Residual stress, σ_0 [MPa]	Ultimate stress, σ_{Ult} [MPa]	Ultimate strain, ϵ_{Ult} [%]	Toughness, U_t [kJ m^{-3}]
0	13.5 ± 2.5	49 ± 12	1.5 ± 0.2	440 ± 60
2.5	09.9 ± 5.4	64 ± 17	1.5 ± 0.3	590 ± 70
7.5	16.1 ± 2.9	77 ± 12	1.8 ± 0.3	860 ± 270
15	11.7 ± 2.9	64 ± 03	1.4 ± 0.1	540 ± 40
22.4	15.9 ± 6.0	73 ± 12	1.1 ± 0.1	510 ± 50

3. Conclusions

We have fabricated freestanding LbL films with encapsulated silver nanowires. The nanowire volume fraction in these films ranges from 2.5 to 22.5%. For the highest volume fraction of silver nanowires, a high Young's modulus of about 6 GPa as well as a high ultimate strength (ranging from 60–80 MPa) has been achieved due to the filler reinforcement effect.

The static fracture toughness reaches 1000 kJ m^{-3} at an intermediate nanowire concentration, $\phi = 7.5\%$. We suggest that these robust, elastic, freestanding nanoscale membranes containing 2D arrays of silver nanowires could serve as prospective sensing elements with peculiar optical and conducting properties for microscopic acoustic, pressure, and photothermal sensors. Indeed, our preliminary studies indicate planar conductivity within these membranes at a certain nanowire volume fraction.^[58] Moreover, the uniform orientation of nanowires or other ordered arrangements could result in LbL films with controlled directional conductivity and optical response.

4. Experimental

Chemicals and Materials: All chemicals for silver nanowire synthesis and LbL assembly were purchased from Aldrich and used as received. These included anhydrous ethylene glycol (EG, 99.8%), AgNO_3 (99+%), PVP (molecular weight $M_w = 130000 \text{ Da}$), PAH ($M_w = 70000 \text{ Da}$), PSS ($M_w = 70000 \text{ Da}$), and CA. Nylon membranes with a pore size of $5 \mu\text{m}$ were purchased from Perkin–Elmer. Freshly cut $1 \text{ cm} \times 2 \text{ cm}$ silicon substrates with a [100] orientation (Semiconductor Processing Co.) were treated with a piranha solution (1:3 (v/v) $\text{H}_2\text{O}_2/\text{H}_2\text{SO}_4$), rinsed thoroughly with Nanopure water ($\sigma > 18.0 \text{ M}\Omega\text{cm}$), and dried under a nitrogen stream [79]. Copper substrates with a $150 \mu\text{m}$ hole and transmission electron microscopy (TEM) copper grids (200 mesh) were purchased from Electron Microscopy Sciences.

Instrumentation: UV-vis spectra were recorded with a UV-1601 spectrometer (Shimadzu). X-ray diffraction patterns were acquired using a Rigaku Miniflex instrument with $\text{Cu K}\alpha$ radiation ($\lambda = 0.154 \text{ nm}$) between $2\theta = 10^\circ$ and 90° . AFM images were collected using a Dimension-3000 instrument in the “light” tapping mode according to the procedure developed in our laboratories [80,81]. The samples were scanned at $0.5\text{--}1.0 \text{ Hz}$ for surface areas between $40 \mu\text{m} \times 40 \mu\text{m}$ and $1 \mu\text{m} \times 1 \mu\text{m}$. The domain height and surface area coverage were determined from cross-sectional and bearing analysis, respectively. Silicon nitride tips with tip radii between $20\text{--}50 \text{ nm}$ and spring constants ranging from $0.01\text{--}50 \text{ N m}^{-1}$ were used in this study. Scanning electron microscopy was conducted in secondary electron scattering mode at 20 keV (JEOL JSM-6060LV).

Silver Nanowire Synthesis: Silver nanowires were synthesized in high yields according to a well-established procedure [59,60,62]. All glassware was washed with soap, aqua regia, and rinsed thoroughly with deionized water. First, a PVP solution (0.36 M , 15 mL) in anhydrous EG was heated under constant stirring at 160°C for a minimum of 1 h . Next, a room-temperature AgNO_3 solution in EG (0.12 M , 7.5 mL) was added dropwise into the hot PVP solution over a period of $10\text{--}15 \text{ min}$. Then, the solution mixture was allowed to stir for another $45\text{--}50 \text{ min}$. After cooling to room temperature, the final opaque gray-green solution containing a white iridescent precipitate was diluted with methanol in a 1:1 ratio. Then, the silver nanowires were precipitated in excess tetrahydrofuran (THF) to remove the majority of EG, PVP, and some low-aspect-ratio nanoparticles. The suspension was left to stand overnight to allow the gray-green material to settle at the bottom of flask. Subsequently, this material was redispersed in methanol. Finally, the silver nanowire solution in methanol was filtered through a pre-weighed $5 \mu\text{m}$ nylon membrane and rinsed multiple times with methanol until the filtrate was transparent. This indicated that the majority of low-aspect-ratio nanoparticles (bright yellow solution) had been removed. The purified gray solution was redispersed in methanol to obtain a concentration of roughly $1\text{--}2 \text{ mg mL}^{-1}$. It was stable if stored in a tightly sealed flask and used within 1 week [82].

LbL Films: The freestanding LbL membranes were fabricated by a spin-assisted layer-by-layer (SA-LbL) assembly process, according to a procedure previously described in the literature [13,68,83–88]. Briefly, a CA droplet ($2.5 \text{ wt}\%$ solution in acetone containing $3 \text{ wt}\%$ water,

$150 \mu\text{L}$) was spin-coated onto a clean silicon wafer. Alternating positive and negative PAH and PSS layers were spin-coated to form ten bottom PAH/PSS bilayers terminated with PAH, followed by casting the Ag nanowire solution in methanol ($1\text{--}2 \text{ mg mL}^{-1}$, $100 \mu\text{L}$ or one drop). The density of the Ag nanowires was controlled by multiple drops of $100 \mu\text{L}$ of the nanowire solution. In between casting steps, the coated surface was rinsed once again with Nanopure water. Upon solution casting, the gray Ag nanowire solution uniformly wet the entire surface, and dried within 30 s . Another ten PAH/PSS bilayers were assembled at the top after rinsing the final nanowire layer twice with Nanopure water. The sample was rinsed twice with Nanopure water after depositing each polyelectrolyte layer. Films with silver nanowires sandwiched between $(\text{PAH/PSS})_{10}\text{PAH}$ films are designated as $(\text{PAH/PSS})_{10}\text{PAH Ag}(\text{PAH/PSS})_{10}\text{PAH}$ (ϕ), where ϕ refers to the volume fraction of nanowires within the central layer. The volume fraction ϕ is calculated as the volume occupied by silver nanowires (assuming a cylindrical cross section) divided by the total volume of the membrane (taking into account the asymmetrical geometry of the membrane discussed in the text). The above procedures were performed in a Class 100 cleanroom.

Finally, the LbL films were cut into approximately $2 \text{ mm} \times 2 \text{ mm}$ squares using a stainless steel microneedle. They were then released by submersion in acetone, which preferentially dissolves the CA layer [89]. For easy deposition on a 3 mm diameter copper substrate with a $150 \mu\text{m}$ opening or on a TEM grid, the floating membranes were transferred into another Petri dish containing Nanopure water. For thickness determination, some membranes were deposited on a silicon substrate and a micrometer-wide scratch mark was made. The membrane thickness was measured by AFM cross-sectional analysis across the edge of the film or across the scratch mark.

Bulging Test: Bulging tests were performed according to procedures described in detail in the literature [90–94]. The bulging tests were performed using a custom-made interferometer equipped with a charge coupled device (CCD) camera (Logitech) and a He–Ne laser ($\lambda = 632.8 \text{ nm}$). Pressures up to 5000 Pa were exerted using a 60 mL syringe regulated by an automatic pump (Kent Scientific Inc.) and monitored with an automatic pressure gauge, DPM 0.1 (SI Pressure Instruments). The bulging test data was analyzed using a model for the elastic deformation of circular membranes, according to the procedure described previously [68].

The LbL membranes freely suspended over a copper substrate with a $150 \mu\text{m}$ hole were first inspected under an optical microscope and a minimal pressure was exerted to check for symmetrical Newton’s ring patterns that indicate membrane homogeneity (Fig. 15 i). While monitoring pressure, the slightly pressurized membrane was allowed to stand idle for a few minutes to ensure the absence of any leaks. The mounted membrane was then tilted at a minimum angle, θ , to form a

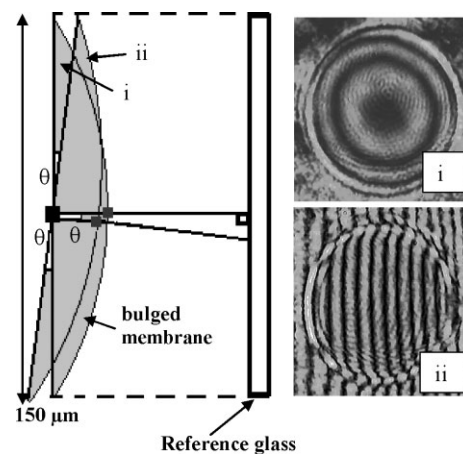


Figure 15. Two types of interference patterns employed in the bulging experiment: i) regular Newton’s rings pattern and ii) linear fringe pattern for a tilted membrane.

vertical interference pattern (Fig. 15 ii, usually about nine fringes). For bulging measurements conducted between 0 and 5000 Pa, the maximum membrane deflection did not exceed 8 μm . Under these conditions, the maximum error due to tilting was about 6 nm, which is within the resolution of the interference pattern ($1/4\lambda$ or 160 nm). During measurements, a transparent crosshair window was laid over the digital image of the membrane such that the central vertical interference pattern coincided with the vertical line of the crosshair. As the pressure increased, the interference pattern moved laterally across the crosshair. Concomitantly, the deflection of the copper substrate was also monitored using a mouse cursor as the target marker. During the course of the experiment, the copper deformed by as much as 40 % with respect to the membrane. At least 40 data points (pressure vs. deflection) were recorded in “real-time” for each bulging measurement for both membrane and copper deflections. The actual membrane deflection was determined by subtracting the copper deflection from the observed membrane deflection. A minimum of three randomly selected specimens were measured for each membrane with different densities of Ag nanowires.

Buckling Test: Buckling tests were conducted to independently evaluate the elastic modulus of LbL membranes from the elastic buckling instability [69,95]. For an isotropic thin membrane, a uniform buckling pattern with a characteristic wavelength, λ , is observed when it is subjected to a critical compressive stress. The spacing of this pattern is directly related to the elastic modulus [71]. To initiate the buckling pattern, a 2 mm \times 2 mm membrane piece was placed over a 0.6 cm \times 0.6 cm \times 0.4 cm PDMS substrate, which was slowly compressed with micrometer-sized increments. The total compressive distance was generally less than 15 μm . The compression was monitored in differential interference contrast (DIC) mode adjusted for maximum contrast. Optical images were captured with a Leica MZ16 microscope in reflection mode. The digital images were Fourier transformed using ImageJ software.

Received: May 16, 2006

Published online: September 12, 2006

- [1] L. H. Sperling, *Polymeric Multicomponent Materials: An Introduction*, Wiley, New York 1997.
- [2] A. Heilmann, in *Polymer Films with Embedded Metal Nanoparticles* (Eds: R. Hull, R. M. Osgood, Jr., J. Parisi), Springer, Berlin 2003.
- [3] G. Decher, *Science* 1997, 277, 1232.
- [4] *Multilayer Thin Films* (Eds: G. Decher, J. B. Schlenoff), Wiley-VCH, Weinheim 2003.
- [5] Y. Lvov, R. Price, B. Gaber, I. Ichinose, *Colloids Surf. A* 2002, 198, 375.
- [6] P. T. Hammond, *Adv. Mater.* 2004, 16, 1271.
- [7] C. Jiang, S. Markutsya, Y. Pikus, V. V. Tsukruk, *Nat. Mater.* 2004, 3, 721.
- [8] A. A. Mamedov, N. A. Kotov, V. Prato, D. M. Guldi, J. P. Wicksted, A. Hirsch, *Nat. Mater.* 2002, 1, 190.
- [9] Y.-C. Chu, C.-C. Wang, C.-Y. Chen, *J. Membr. Sci.* 2005, 247, 201.
- [10] C. Jiang, V. V. Tsukruk, *Adv. Mater.* 2006, 18, 829.
- [11] Y. Lu, G. L. Liu, L. P. Lee, *Nano Lett.* 2005, 5, 5.
- [12] a) H. Ko, C. Jiang, V. V. Tsukruk, *Chem. Mater.* 2005, 17, 5489. b) C. Jiang, S. Markutsya, H. Shulha, V. V. Tsukruk, *Adv. Mater.* 2005, 17, 1669.
- [13] C. Jiang, B. M. Rybak, S. Markutsya, P. E. Kladitis, V. V. Tsukruk, *Appl. Phys. Lett.* 2005, 86, 121 912.
- [14] C. Jiang, M. McConney, S. Singamaneni, E. Merrick, Y. Chen, J. Zhao, L. Zhang, V. V. Tsukruk, *Chem. Mater.* 2006, 18, 2632.
- [15] G. Schmid, *Nanoparticles from Theory to Application*, Wiley-VCH, Weinheim 2004.
- [16] K.-S. Chou, Y.-S. Lai, *Mater. Chem. Phys.* 2004, 83, 82.
- [17] B. Wiley, T. Herricks, Y. Sun, Y. Xia, *Nano Lett.* 2004, 4, 1733.
- [18] J. Chen, F. Sacki, B. J. Wiley, H. Cang, M. J. Cobb, Z.-Y. Li, L. Au, H. Zhang, M. B. Kimmey, X. Li, Y. Xia, *Nano Lett.* 2005, 5, 473.
- [19] C. J. Murphy, T. K. Sau, A. M. Gole, C. J. Orendorff, J. Gao, L. Gou, S. E. Hunyadi, T. Li, *J. Phys. Chem. B* 2005, 109, 13 857.
- [20] Y. Sun, Y. Yin, B. T. Mayers, T. Herricks, Y. Xia, *Chem. Mater.* 2002, 14, 4736.
- [21] Y. Gao, P. Jiang, L. Song, L. Liu, X. Yan, Z. Zhou, D. Liu, J. Wang, H. Yuan, Z. Zhang, X. Zhao, X. Dou, W. Zhou, G. Wang, S. Xie, *J. Phys. D: Appl. Phys.* 2005, 38, 1061.
- [22] Y. Sun, B. Gates, B. T. Mayers, Y. Xia, *Nano Lett.* 2002, 2, 165.
- [23] M. H. Huang, A. Choudrey, P. Yang, *Chem. Commun.* 2000, 1063.
- [24] K. K. Caswell, C. M. Bender, C. J. Murphy, *Nano Lett.* 2003, 3, 667.
- [25] Y. Gao, L. Song, P. Jiang, L. F. Liu, X. Q. Yan, Z. P. Zhou, D. F. Liu, J. X. Wang, H. J. Yuan, Z. X. Zhang, X. W. Zhao, X. Y. Dou, W. Y. Zhou, G. Wang, S. S. Xie, H. Y. Chen, J. Q. Li, *J. Cryst. Growth* 2005, 276, 606.
- [26] M. Giersig, I. Pastoriza-Santos, L. M. Liz-Marzán, *J. Mater. Chem.* 2004, 14, 607.
- [27] S.-H. Zhang, Z.-Y. Jiang, Z. X. Xie, X. Xu, R.-B. Huang, L.-S. Zheng, *J. Phys. Chem. B* 2005, 209, 9416.
- [28] D. Zhang, L. Qi, J. Yang, J. Ma, H. Cheng, L. Huang, *Chem. Mater.* 2004, 16, 872.
- [29] J.-Y. Piquemal, G. Viau, P. Beaunier, F. Bozon-Verduraz, F. Fiévet, *Mater. Res. Bull.* 2003, 38, 389.
- [30] G. Viau, J.-Y. Piquemal, M. Esparicca, U. Diane, N. Chakroune, F. Warmount, F. Fiévet, *Chem. Commun.* 2003, 2216.
- [31] Y. Xiong, Y. Xie, C. Wu, J. Yang, Z. Li, F. Xu, *Adv. Mater.* 2003, 15, 405.
- [32] X. Sun, Y. Li, *Adv. Mater.* 2005, 17, 2626.
- [33] J.-H. Park, S.-G. Oh, B.-W. Jo, *Mater. Chem. Phys.* 2004, 87, 301.
- [34] A. Machulek, Jr., H. Paulo, H. P. Moisés de Oliviera, M. H. Gehlen, *Photochem. Photobiol. Sci.* 2003, 2, 921.
- [35] X. Zheng, L. Zhu, A. Yan, X. Wang, Y. Xie, *J. Colloid Interface Sci.* 2003, 268, 357.
- [36] A. Callegari, D. Tonti, M. Chergui, *Nano Lett.* 2003, 3, 1565.
- [37] S. Chen, D. L. Carroll, *J. Phys. Chem. B* 2004, 108, 5500.
- [38] K. Zou, X. H. Zhang, X. F. Duan, X. M. Meng, S. K. Wu, *J. Cryst. Growth* 2004, 273, 285.
- [39] B. H. Hong, S. C. Bae, C.-W. Lee, S. Jeong, K. S. Kim, *Science* 2001, 294, 348.
- [40] B. M. Rybak, M. Ornatska, K. N. Bergman, K. L. Genson, V. V. Tsukruk, *Langmuir* 2006, 22, 1027.
- [41] C. Fischer, A. Heller, G. Dube, *Mater. Res. Bull.* 1989, 21, 1271.
- [42] F. Fievet, J. P. Lagier, B. Blin, B. Beaudoin, M. Figlarz, *Solid State Ionics* 1989, 32, 198.
- [43] C. Ducamp-Sanguesa, R. Herrera-Urbina, M. Figlarz, *Solid State Ionics* 1993, 63, 25.
- [44] Y. Sun, B. T. Mayers, T. Herricks, Y. Xia, *Nano Lett.* 2003, 3, 955.
- [45] Y. Gao, P. Jiang, D. F. Liu, H. J. Yuan, X. Q. Yan, Z. P. Zhou, J. X. Wang, L. Song, L. F. Liu, W. Y. Zhou, G. Wang, C. Y. Wang, S. S. Xie, *Chem. Phys. Lett.* 2003, 380, 146.
- [46] J. B. Jackson, N. J. Halasa, *J. Phys. Chem. B* 2001, 105, 2743.
- [47] J. P. Kottmann, O. J. F. Martin, D. R. Smith, S. Schultz, *Phys. Rev. B: Condens. Matter* 2001, 64, 235 402.
- [48] R. M. Dickson, L. A. Lyon, *J. Phys. Chem. B* 2000, 104, 6095.
- [49] D. H. Jeong, Y. X. Zhang, M. Moskovits, *J. Phys. Chem. B* 2004, 108, 12 724.
- [50] G. Schider, J. R. Krenn, A. Hohenau, H. Diltbacher, A. Leitner, F. R. Aussenegg, W. L. Schaich, I. Puscasu, B. Monacelli, G. Boreman, *Phys. Rev. B: Condens. Matter* 2003, 68, 155 427.
- [51] S. J. Lee, A. R. Morrill, M. Moskovits, *J. Am. Chem. Soc.* 2006, 128, 2200.
- [52] K. Aslan, Z. Leonenko, J. R. Lakowicz, C. D. Geddes, *J. Phys. Chem. B* 2005, 109, 3157.
- [53] C. Orendorff, A. Gole, T. K. Sau, C. J. Murphy, *Anal. Chem.* 2005, 77, 3261.
- [54] R.-L. Zong, J. Zou, Q. Li, B. Du, B. Li, M. Fu, X.-W. Qi, L.-T. Li, S. Buddhudu, *J. Phys. Chem. B* 2004, 108, 16 713.
- [55] N. I. Kovtyukhova, T. E. Mallouk, *Chem. Eur. J.* 2002, 8, 4354.
- [56] N. I. Kovtyukhova, B. R. Martin, J. K. N. Mbindyo, P. A. Smith, B. Razavi, T. S. Mayer, T. E. Mallouk, *J. Phys. Chem. B* 2001, 105, 8762.

- [57] Y. T. Pang, G. W. Meng, Q. Fang, L. D. Zhang, *Nanotechnology* **2003**, *14*, 20.
- [58] R. Gunawidjaja, C. Jiang, H. Ko, V. V. Tsukruk, *Adv. Mater.*, in press.
- [59] R. F. Aroca, P. J. G. Goulet, D. S. dos Santos, R. A. Alvarez-Puebla, O. N. Oliviera, Jr., *Anal. Chem.* **2005**, *77*, 378.
- [60] A. Tao, F. Kim, C. Hess, J. Goldberger, R. He, Y. Sun, Y. Xia, P. Yang, *Nano Lett.* **2003**, *3*, 1229.
- [61] Y. Gao, P. Jiang, D. F. Liu, H. J. Yuan, X. Q. Yan, Z. P. Zhou, J. X. Wang, L. Song, L. F. Liu, W. Y. Zhou, G. Wang, C. Y. Wang, S. S. Xie, J. M. Zhang, D. Y. Shen, *J. Phys. Chem. B* **2004**, *108*, 12 877.
- [62] Y. Sun, Y. Xia, *Adv. Mater.* **2002**, *14*, 833.
- [63] N. R. Jana, L. Gearheart, C. J. Murphy, *Chem. Commun.* **2001**, 617.
- [64] D. Chen, L. Gao, *J. Cryst. Growth* **2004**, *264*, 216.
- [65] J. Gasga-Reyes, J. L. Elechiguerra, C. Liu, A. Camacho-Bragado, J. M. Montejano-Carrizales, M. Jose Yacaman, *J. Cryst. Growth* **2006**, *286*, 162.
- [66] S. Jayaraman, R. L. Edwards, K. J. Hemker, *J. Mater. Res.* **1999**, *14*, 688.
- [67] C. Poilane, P. Delobelle, C. Lexcellent, S. Hayashi, H. Tobushi, *Thin Solid Films* **2000**, *379*, 156.
- [68] S. Markutsya, C. Jiang, Y. Pikus, V. V. Tsukruk, *Adv. Funct. Mater.* **2005**, *15*, 771.
- [69] A. L. Volynskii, S. Bazhenov, O. V. Lebedeva, N. F. Bakeev, *J. Mater. Sci.* **2000**, *35*, 547.
- [70] S. N. Magonov, *Surface Analysis with STM and AFM: Experimental and Theoretical Aspects of Image Analysis*, VCH, Weinheim **1996**.
- [71] A. J. Nolte, M. F. Rubner, R. E. Cohen, *Macromolecules* **2005**, *38*, 5367.
- [72] D. D. Agarwal, L. J. Broutman, *Analysis and Performance of Fiber Composites*, 2nd ed., Wiley, New York **1990**, p. 129.
- [73] H. Ko, C. Jiang, H. Shulha, V. V. Tsukruk, *Chem. Mater.* **2005**, *17*, 2490.
- [74] X. Li, H. Gao, C. J. Murphy, K. K. Caswell, *Nano Lett.* **2003**, *3*, 1495.
- [75] O. Kraft, C. A. Volkert, *Adv. Mater.* **2001**, *3*, 99.
- [76] A. J. Kalkman, A. H. Vebruggen, G. C. A. M. Janssen, *Rev. Sci. Instrum.* **2003**, *74*, 1383.
- [77] D. K. Felbeck, A. G. Atkins, in *Strength and Fracture of Engineering Solids*, Prentice-Hall, Englewood Cliffs, NJ **1984**.
- [78] S. Hashemi, *J. Mater. Sci.* **1997**, *32*, 1563.
- [79] V. V. Tsukruk, V. N. Bliznyuk, *Langmuir* **1998**, *14*, 446.
- [80] V. V. Tsukruk, *Rubber Chem. Technol.* **1997**, *70*, 430.
- [81] V. V. Tsukruk, D. H. Reneker, *Polymer* **1995**, *36*, 1791.
- [82] J. L. Elechiguerra, L. Larios-Lopez, C. Liu, D. Garcia-Gutierrez, A. Camacho-Bragado, M. J. Yacaman, *Chem. Mater.* **2005**, *17*, 6042.
- [83] C. Jiang, V. V. Tsukruk, *Soft Matter* **2005**, *1*, 334.
- [84] C. Jiang, W. Y. Lio, V. V. Tsukruk, *Phys. Rev. Lett.* **2005**, *95*, 115 503.
- [85] C. Jiang, S. Markutsya, V. V. Tsukruk, *Langmuir* **2004**, *20*, 882.
- [86] C. Jiang, H. Ko, V. V. Tsukruk, *Adv. Mater.* **2005**, *17*, 2127.
- [87] J. Cho, K. Char, J.-D. Hong, K.-B. Lee, *Adv. Mater.* **2001**, *13*, 1076.
- [88] P. A. Chiarelli, M. S. Johal, J. L. Casson, J. B. Roberts, J. M. Robinson, H.-L. Wang, *Adv. Mater.* **2001**, *13*, 1167.
- [89] A. A. Mamedov, N. A. Kotov, *Langmuir* **2000**, *16*, 5530.
- [90] H. Xu, F. Heger, F. Mallwitz, M. Blankenhagel, C. Peyratout, W. A. Goedel, *Macromol. Symp.* **2002**, *177*, 175.
- [91] F. Mallwitz, W. A. Goedel, *Angew. Chem. Int. Ed.* **2001**, *40*, 2645.
- [92] W. A. Goedel, R. Heger, *Langmuir* **1998**, *25*, 3470.
- [93] J. W. Beams, in *Structure and Properties of Thin Solid Films* (Eds: C. A. Neugebauer, J. B. Newkirk, D. A. Vermilyea), Wiley, New York **1959**, p. 183.
- [94] J. J. Vlasak, W. D. Nix, *J. Mater. Res.* **1992**, *7*, 3242.
- [95] C. M. Stafford, C. Harrison, K. L. Beers, A. Karim, E. J. Amis, M. R. Vanlandingham, H. C. Kim, W. Volksen, R. D. Miller, E. E. Simonyi, *Nat. Mater.* **2004**, *3*, 545.